

A UNIFIED LENSE-THIRRING PRECESSION MODEL FOR OPTICAL AND X-RAY QUASI-PERIODIC OSCILLATIONS IN BLACK HOLE BINARIES

ALEXANDRA VELEDINA¹, JURI POUTANEN¹, AND ADAM INGRAM²

¹Astronomy Division, Department of Physics, P.O. Box 3000, FI-90014 University of Oulu, Finland;
 alexandra.veledina@oulu.fi, juri.poutanen@oulu.fi

²Astronomical Institute “Anton Pannekoek”, University of Amsterdam, Postbus 94249, 1098 GE Amsterdam, The Netherlands

Received 2013 June 10; accepted 2013 October 9; published 2013 ???

ABSTRACT

Recent observations of accreting black holes reveal the presence of quasi-periodic oscillations (QPO) in the optical power density spectra. The corresponding oscillation periods match those found in the X-rays, implying a common origin. Among the numerous suggested X-ray QPO mechanisms, some may also work in the optical. However, their relevance to the broadband – optical through X-ray – spectral properties have not been investigated. For the first time, we discuss the QPO mechanism in the context of the self-consistent spectral model. We propose that the QPOs are produced by Lense-Thirring precession of the hot accretion flow, whose outer parts radiate in the optical wavelengths. At the same time, its innermost parts are emitting the X-rays, explaining the observed connection of QPO periods. We predict that the X-ray and optical QPOs should be either in phase or shifted by half a period, depending on the observer position. We investigate the QPO harmonic content and find that the variability amplitudes at the fundamental frequency are larger in the optical, while the X-rays are expected to have strong harmonics. We then discuss the QPO spectral dependence and compare the expectations to the existing data.

Subject headings: accretion, accretion disks – black hole physics – radiation processes: nonthermal – X-rays: binaries

1. INTRODUCTION

Accreting black holes (BH) remain among the most fascinating objects being studied since the very beginning of the X-ray era. The observed X-ray radiation is variable on a wide range of timescales, displaying dramatic changes in spectral shape between the power law dominated hard state and the quasi-thermal soft state over timescales of weeks (Zdziarski & Gierliński 2004). Strong variability is also seen on far shorter (down to ~ 10 ms) timescales. Among the most prominent features commonly observed in the power spectral density (PSD) of BH binaries are low-frequency quasi-periodic oscillations (QPOs) (Remillard & McClintock 2006; Done et al. 2007), with a characteristic frequency which evolves from ~ 0.1 –10 Hz at the spectral transitions from the hard to soft state. A growing number of low-mass X-ray binaries have also been found to exhibit similar QPOs in the optical and UV PSDs (Motch et al. 1983, 1985; Imamura et al. 1990; Steiman-Cameron et al. 1997; Hynes et al. 2003; Durant et al. 2009; Gandhi et al. 2010). The optical, UV and X-ray QPOs in XTE J1118+480 have been observed to share a common (within uncertainties) characteristic frequency whilst evolving over nearly two months of observations (Hynes et al. 2003). In the X-rays, the QPO frequency is correlated with the low-frequency break of the broadband noise (Wijnands & van der Klis 1999; Belloni et al. 2002). Hints of such a correlation in the optical can also be found in the existing data (Gandhi et al. 2010; Hynes et al. 2003), however the significance is too low to make any conclusive statements. It is therefore suggestive that the X-ray and optical QPOs are formed by a common mechanism which is somehow related to the production of aperiodic variability (broadband noise).

However, there is no consensus in the literature as to the origin of the X-ray QPO and so far no optical QPO mechanism has been suggested.

Proposed X-ray QPO mechanisms are generally based either on the misalignment of the BH and binary system spins (e.g., Stella & Vietri 1998) or on oscillation modes of the accretion flow itself (e.g., Wagoner et al. 2001). Many of them, however, discuss the QPO production separately and do not consider its relation to the aperiodic X-ray variability. Probably the most promising QPO model to date was proposed in Ingram et al. (2009), where the oscillations arise from the precession of orbits around the BH due to misalignment of the BH and orbital spins, known as Lense-Thirring precession. Similar models proposed earlier considered the precession of a test mass (Schnittman et al. 2006), leading to a strong dependence of the predicted QPO frequency on BH spin, inconsistent with the observations. The model of Ingram et al. (2009) considers the precession of the entire hot flow, which leads to a much weaker spin dependence. We note that the precession of the entire flow as a solid body can only be possible in the case of a hot geometrically thick accretion flow (Fragile et al. 2007), while a cold thin disk would produce a steady warp in the plane perpendicular to the BH spin (Bardeen & Petterson 1975; Kumar & Pringle 1985). Recently, it was shown that the physical parameters of the hot flow picked to match the observed QPO frequency are also consistent with those required to produce the characteristic frequencies of the broad band noise (Ingram & Done 2011), thus a global connection between the QPO and aperiodic variability was established.

This variability model ultimately requires a geometry

where the cold (Shakura & Sunyaev 1973) accretion disk is truncated at some radius and the BH vicinity is occupied by some type of the hot accretion flow (*the truncated disk model*; Esin et al. 1997; Poutanen et al. 1997). The power law component of the X-ray spectrum can be understood in this geometry as Compton up-scattering of cold seed photons by hot electrons in the flow. The seed photons are often assumed to be provided by the disk, however in the hard state when the truncation radius is large ($\sim 30R_S$ where $R_S = 2GM/c^2$ is the Schwarzschild radius), the luminosity of disk photons incident on the flow is insufficient to reproduce the observed spectra and an additional source of seed photons is required. This can be provided by synchrotron radiation in the flow. Compton up-scattering of the resulting internally produced seed photons (the synchrotron self-Compton mechanism) can successfully reproduce the observed hard state spectra (Malzac & Belmont 2009; Poutanen & Vurm 2009). Let us note that an array of accretion geometries can explain the observed spectra but the Lense-Thirring QPO model is compatible only with the truncated disk model considered here.

Lately, it was shown that the hot flow synchrotron emission can contribute to the optical and even IR (OIR) wavelengths (Veledina et al. 2013), thus these wavelengths are tightly connected to the X-ray component. Hence, the spectral model also predicts the connection between the OIR and the X-ray aperiodic variability. However, simultaneous analysis of light-curves in these wavelengths (Motch et al. 1983; Kanbach et al. 2001; Hynes et al. 2003; Durant et al. 2008; Gandhi et al. 2010) has revealed a complicated connection between them, which can be understood if one considers several components contributing to the optical (Veledina et al. 2011), namely the hot accretion flow and the reprocessed radiation. Additionally, the jet optically thin synchrotron emission can also be significant (e.g. Casella et al. 2010). These three components presumably can be responsible for the OIR QPOs.

In Section 2 we develop a quantitative model for the low-frequency OIR and X-ray QPOs, which are produced by Lense-Thirring precession of a hot accretion flow. We make predictions for the OIR QPO profiles and compare them to those expected in the X-rays. We then calculate the phase-lags and harmonic content expected from this model. In Section 3, we discuss the limitations of the model and possible improvements and compare the model predictions with the data. We summarize our findings in Section 4.

2. HOT FLOW QPO MODEL

2.1. Assumptions

In this section, we outline our assumptions. We consider a hot accretion flow extending from some inner radius to the truncation radius of the cold outer disk and a spin axis misaligned with that of the BH by some angle β . In the Kerr metric, test particle orbits out of the plane of BH rotation undergo Lense-Thirring precession due to the dragging of inertial frames, with a frequency $\nu_{LT}(R) \propto R^{-3}$. In the case of a hot accretion flow, this differential precession creates a warp which propagates through the flow on a time scale shorter than the precession period. This can cause the entire flow to

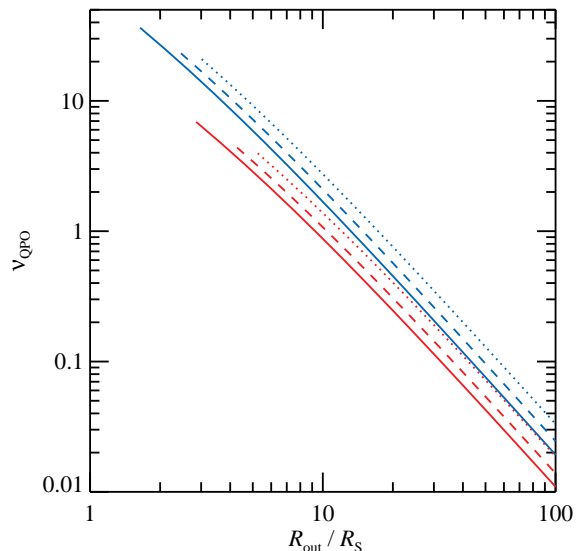


Figure 1. Possible QPO frequencies as function of the hot flow outer radius (R_{out}), calculated for a $10M_{\odot}$ BH according to equation (43) of Fragile et al. (2007), with inner radius equal to $R_{in} = 1.5 (H/R)^{-4/5} a^{2/5} R_S$ (Lubow et al. 2002), for spins of $a = 0.2$ (solid), 0.3 (dashed) and 0.5 (dotted). Red lines correspond to $H/R = 0.2$ and blue lines correspond to $H/R = 0.4$.

precess as a solid body at a frequency given by a surface density weighted average of $\nu_{LT}(R)$ (Fragile et al. 2007). If the flow is assumed to extend from the disk truncation radius to the inner most stable circular orbit, the dependence of the precession frequency on BH spin is too strong and the maximum precession frequency is too high to be consistent with observations. In order to put the Lense-Thirring frequencies into the observed QPO range, from ~ 0.03 Hz (Vikhlinin et al. 1994) up to ~ 13 Hz (Remillard et al. 1999), one needs to account for the torque created by frame dragging, which truncates the inner flow at a fairly large (inner) radius ($\gtrsim 3R_S$, see equation 22 of Lubow et al. 2002, where $x = 1$ should be taken) and effectively cancels out much of the spin dependence of precession (Ingram et al. 2009). This effect has since been seen in simulations (Fragile 2009). We reproduce the dependence of the QPO frequency on the outer radius of the hot flow in Figure 1. Since we aim to model the hard state, we assume a fairly large truncation radius of $R_{out} = 30R_S$, leading to a predicted precession frequency consistent with the observed QPO frequency in this state ($\lesssim 0.3$ Hz). When R_{out} decreases (corresponding to transition to the hard-intermediate state), ν_{QPO} grows up to 5–20 Hz.

Although the condition on the flow height-to-radius ratio, H/R , for the fast propagation of warps which allows solid body precession is $H/R > \alpha \sim 0.1$, where α is the dimensionless viscosity parameter (Papaloizou & Pringle 1983; Fragile et al. 2007), H/R significantly less than unity is likely (Kato et al. 2008). Thus, we approximate the flow as a flat disk. This approximation is satisfactory for systems with a low enough inclination for the flow never to be seen edge-on at any point in the precession cycle. We illustrate in our plots the regions of parameter space where this condition is not met. In order to calculate the emitted flux, we must make an assumption about the radial dependence of energy dissipation per unit area in the flow. We assume the standard profile for

a thin disk (Shakura & Sunyaev 1973)

$$q(R) \propto R^{-3} \sqrt{1 - \frac{R_{\text{in}}}{R}}, \quad (1)$$

where R_{in} is the hot flow inner radius, which we assume to be equal $3R_S$ (for parameters in Figure 1 it takes the values $\sim 2-5R_S$). The profile is not strictly appropriate for a hot flow in general relativity (Novikov & Thorne 1973; Kato et al. 2008), but is fine for illustration in the absence of a standard equivalent for hot flows. The details of the energy dissipation profile do not play an important role. For calculations of the angular dependence of the emergent radiation we take into account relativistic effects using the Schwarzschild metric (see Sect. 2.3). Since we are considering Lense-Thirring precession, this is obviously only an approximation to the more appropriate Kerr metric. However, the Schwarzschild metric provides a very good approximation at distances more than $3R_S$ from the BH.

We take into account only direct images, because the higher-order images are much weaker. The reason is that the hot flow we consider has optical depth of the order of unity, thus most of the photons initially emitted away from the observer would be blocked by the flow itself (or by the outer cold disk). The only possibility for those photons to reach the observer is to go through the rather small gap between the inner edge of the hot flow ($\sim 3R_S$) and the black hole. In addition, photons coming in the higher-order images are generally emitted at grazing angles to the flow surface and therefore their strength is diminished by the corresponding cosine factor. In order to estimate the accuracy of the described approach, we compared fluxes obtained using our light tracing procedure with those obtained using the GEOKERR code in Kerr geometry (Dexter & Agol 2009; Adam Ingram et al., in prep.) including all higher-order images, but accounting for obscuration by the hot flow and the outer cold disk. For the parameters considered in this work, we find our results to be accurate within a few per cent for any spin value up to $a = 0.998$, and for more realistic spins of $a = 0.3, 0.5$ the difference is below 1%.

2.2. Geometry

Figure 2 shows the geometry we consider for the precessing hot accretion flow. We define the coordinate system xyz tied to the binary orbital plane and the system $x'y'z'$, associated with the BH spin. The z -axis is perpendicular to the binary orbital plane, z' is aligned with the BH spin and β is the angle between them. The x -axis is defined by the intersection of the orbital plane and the plane formed by the z and z' axes (i.e. the projection of the z' -axis onto the y -axis is always zero). Finally, the x' -axis also belongs to the plane formed by vectors z and z' , and forms angle β with the x -axis (i.e. $y' = y$). The position of the observer is described by the vector \hat{o} which, in xyz coordinates, is given by

$$\hat{o} = (\sin i \cos \Phi, \sin i \sin \Phi, \cos i), \quad (2)$$

where i is the binary inclination and Φ is the azimuth of the observer measured from the x -axis. The instantaneous normal to the hot flow is denoted by \hat{n} . It precesses around the BH spin axis (z') with the precession angle ω measured from the x' -axis. Thus \hat{n} aligns with

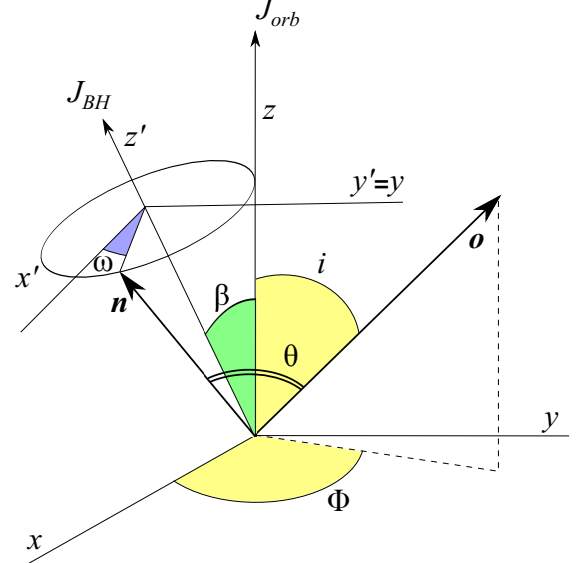


Figure 2. Schematic representation of the hot flow producing X-ray and optical QPOs. Coordinate systems connected with the orbital plane xyz and with the BH spin $x'y'z'$ are shown. Plane xy coincides with the orbital plane and y is parallel to y' . Axis z' is aligned with the BH spin, which is inclined by the angle β to the orbital spin. Position of the observer \hat{o} is described by the azimuthal angle Φ and binary inclination i . The current position of the hot flow normal \hat{n} is characterized by the precession angle (phase) ω . Relative to the direction to the observer, it makes an angle θ , which depends on ω .

the z -axis when $\omega = \pi$ and has a maximal misalignment of 2β when $\omega = 0$. It is given, in $x'y'z'$ coordinates, by $\hat{n} = (\sin \beta \cos \omega, \sin \beta \sin \omega, \cos \beta)$. Note, we use a hat to denote unit vectors throughout.

We are interested in the orientation of the hot flow surface relative to the observer, namely the scalar product $\hat{o} \cdot \hat{n} = \cos \theta$. In order to calculate it, we write \hat{n} in xyz coordinates by rotating the $x'y'z'$ coordinate system counter-clockwise by angle β around the y' -axis to get

$$\hat{n} = (\sin \beta \cos \beta (1 + \cos \omega), \sin \beta \sin \omega, \cos^2 \beta - \sin^2 \beta \cos \omega). \quad (3)$$

Thus, the equation for $\cos \theta$ is

$$\cos \theta = \sin \beta \cos \beta \sin i \cos \Phi (1 + \cos \omega) + \sin \beta \sin \omega \sin i \sin \Phi + \cos i (\cos^2 \beta - \sin^2 \beta \cos \omega). \quad (4)$$

2.3. Formalism

We consider a simplified problem with a precessing flat disk (slab). The specific flux observed far from the BH from a ring of thickness dR at radius R in the direction that makes an angle θ to the surface normal can be expressed as

$$dF_E(R, \theta) = \frac{R dR}{D^2} q_E(R) f(R, \theta). \quad (5)$$

Here, D is the distance to the observer, $q_E(R)$ is the surface flux per energy interval at a given radius and the factor $f(R, \theta)$ accounts for the angular dependence of the observed flux. The latter factor depends on the spectral slope of the radiation.

The flux observed from the whole hot flow is then

$$F_E(\theta) = \frac{\int q_E(R) R dR}{D^2} \bar{f}(\theta), \quad (6)$$

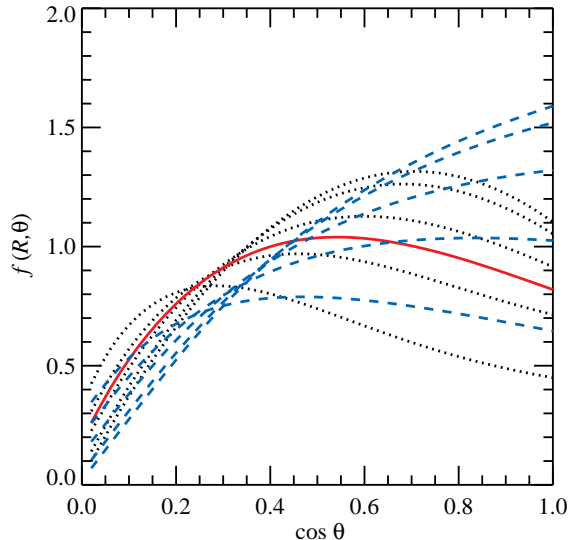


Figure 3. Angular dependence of the observed flux $f(R, \theta)$ as a function of the angle between the observer direction and the normal to the flow. The black dotted lines represent result for the X-ray emission pattern (equation 8) corresponding to Comptonization in an optically translucent flow. The blue dashed lines correspond to the partially self-absorbed synchrotron emission expected in the optical (given by the pattern from equation 9). Curves from the top to the bottom correspond to $R/R_S = 100, 30, 10, 5$ and 3 . The solid red line corresponds to the flux $\bar{f}(\theta)$ from the accretion flow between 3 and $30R_S$ emitting the X-rays with the standard emissivity profile (1).

where we introduced the radially averaged angular factor:

$$\bar{f}(\theta) = \frac{\int q_E(R) R dR f(R, \theta)}{\int q_E(R) R dR}. \quad (7)$$

In general, the specific intensity emerging from a surface element depends on the zenith angle ζ' (primed quantities in the comoving frame). We consider here two cases for the emission pattern from the flow surface:

1. X-ray emission from accreting BHs is produced by Comptonization in an optically translucent flow with Thomson optical depth $\tau \sim 1$. In this case, the angular dependence of the specific intensity can approximately be described by (Poutanen & Gierliński 2003)

$$I'(\zeta') \propto 1 + b \cos \zeta', \quad (8)$$

where $b \approx -0.7$ (for exact solutions see Sunyaev & Titarchuk 1985; Viironen & Poutanen 2004).

2. Optical synchrotron radiation is produced in the outer parts of the flow, in a partially self-absorbed regime. The dominant contribution to the observed flux comes from those parts, which have an optical depth for synchrotron self-absorption $\tau_{SA} \sim 1$. Assuming a tangled magnetic field and homogeneous source function throughout the vertical extent of the flow, the intensity of radiation can be expressed as

$$I'(\zeta') \propto 1 - \exp(-\tau_{SA}/\cos \zeta'). \quad (9)$$

We assume that the emergent spectrum from all surface elements is a power law with photon index $\Gamma =$

1.7 for the X-rays and $\Gamma = 1$ for the optical emission. This allows us to approximate the energy dissipation profile as $q_E(R) \propto q(R)$. To compute the factor $f(R, \theta)$ we take into account gravitational redshift, Doppler effect, relativistic aberration, time dilation and light bending in the Schwarzschild metric following techniques presented by Poutanen & Gierliński (2003) and Poutanen & Beloborodov (2006). Figure 3 shows the resulting angular flux dependence with X-rays and optical represented by black dotted and blue dashed lines, respectively. We plot the function $f(R, \theta)$ for narrow rings at $R/R_S = 100, 30, 10, 5$ and 3 from top to bottom. We also show (by red solid line) the angular distribution of the flux from the accretion flow spread from 3 to $30R_S$, $\bar{f}(\theta)$, emitting the X-rays according to the standard profile given by equation (1). At large radii $R \gtrsim 30R_S$, the relativistic effects are negligible resulting in the angular dependence $f(R, \theta) \propto I'(\theta) \cos \theta$.

2.4. Results

As a first step, we take the X-ray and optical emission to originate from narrow rings with $R = 5R_S$ and $R = 30R_S$, respectively, and compute corresponding QPO waveforms. We set $\beta = 10^\circ$ and $i = 60^\circ, 80^\circ$. The profiles $f(R, \theta)$ (with θ given by equation (4)) are shown in Figure 4 for four different observer azimuths: $\Phi = 0^\circ, 60^\circ, 120^\circ$ and 180° . Again, the black dotted lines are X-rays and the blue dashed line represents the optical. Clearly the phase difference between optical and X-ray profiles depends on the observer's azimuth and inclination: for $i = 60^\circ$ and large Φ the two light-curves are in phase, while for low Φ they are 180° out of phase. This is because the range of $\cos \theta$ covered as the precession angle ω unwinds from 0 to 2π depends on the chosen set of parameters (β, i, Φ) . The range of $\cos \theta$ for every case is shown in Figure 4 with a green dash-dotted line. For small $\cos \theta$ (panels c and d), both optical and X-ray observed fluxes are increasing functions of $\cos \theta$ (see Figure 3), while for large $\cos \theta$ (panels a and b) optical flux is a growing and X-ray flux is a decreasing function of $\cos \theta$. The later is reflected in the anti-correlation of the two light-curves.

For inclinations $i \gtrsim 80^\circ$, eclipses are possible when the observer is situated at the opposite side from the BH spin projection on the orbital plane, i.e. at $\Phi > 90^\circ$. In such a situation, the harmonic content is dramatically increased and the X-ray and optical light curves are always in phase, as here $\cos \theta < 0.5$ (thus both fluxes have monotonic dependence on $\cos \theta$, see Figure 3). However, we need to keep in mind that at such large inclinations the central source might be blocked completely by the outer rim of the cold disk.

We note that the amplitude of the optical QPO for every Φ is higher than in the X-rays. Again, the behavior can be understood from Figure 3: the dependence of the optical flux (blue dashed line at $30R_S$) on $\cos \theta$ is much stronger than that in the X-rays (black dotted line at $5R_S$). This occurs both due to the different emission pattern and because the relativistic effects are stronger at smaller R (due to stronger gravitational curvature and faster Keplerian motion).

For the cases (b)–(d), the X-ray flux maximum is reached not when $\cos \theta$ is maximal, i.e. when the flow is mostly face-on, but when it is inclined at a larger an-

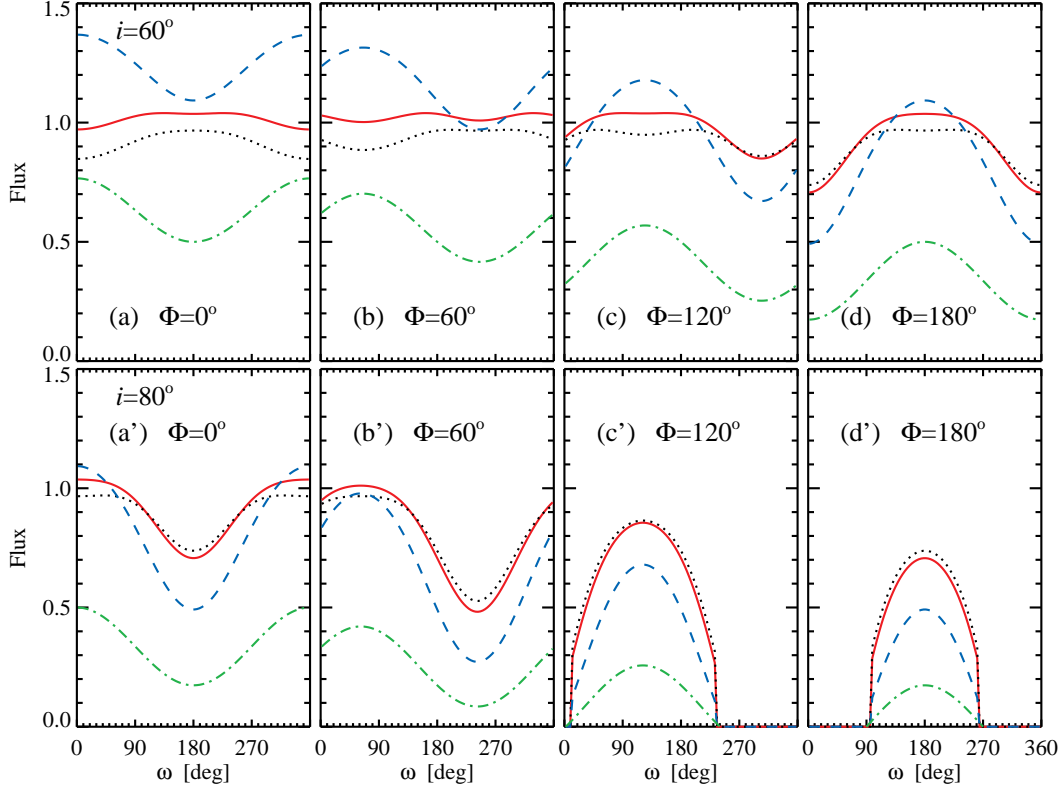


Figure 4. Possible QPO waveforms for the four cases of the observer's azimuthal angle. The parameters are: $\beta = 10^\circ$, $i = 60^\circ$ (upper panels) and $i = 80^\circ$ (lower panels). X-ray profiles are calculated for a ring at $R = 5R_S$ (black dotted lines) and for the full hot flow extending from 3 to $30R_S$ (red solid lines). The optical profiles are for $R = 30R_S$ (blue dashed lines). Green dash-dotted lines represent variations of $\cos \theta$ for each case.

gle (see Figure 3). This leads to the double-peak structures in the X-ray profiles, unlike in the optical (optical flux reaches maximum only at maximal $\cos \theta$, i.e. when the flow is mostly face-on). This gives the X-ray QPO profiles a stronger harmonic content than the optical.

The X-ray light curves expected from the whole hot flow occupying the region 3– $30R_S$ can be computed from the factor $\bar{f}(\theta)$ (with θ given by equation (4)). They are shown by red solid lines in Figure 4. We see that their behavior is very similar to that corresponding to a narrow ring at $5R_S$. This is due to the similarities in the angular dependence of the fluxes (see Figure 3, solid line and dotted line corresponding to $5R_S$). The emission pattern from a ring at $\sim 7R_S$ would be nearly identical to that of the whole extended flow, and so assuming all of the flux to come from close to this radius provides a good approximation.

We analyze the harmonic content of our light curves by directly computing Fourier coefficients. We show the fractional root-mean-square (RMS) variability amplitudes of the first harmonic (referred to below as the fundamental) and the second harmonic (hereafter referred to as the harmonic) as the contour plots at the plane observer azimuth Φ – observer inclination i (Figure 5). The azimuthal angle spans the interval from 0 to 180° , because the results depend on $\cos \Phi$ only. The X-rays are assumed to be coming from the whole flow extending from 3 to $30R_S$ with a standard emissivity profile given by equation (1). The X-ray RMS is shown by red lines. The optical again is assumed coming from $30R_S$ and its RMS is shown by blue lines.

Behavior of the X-ray and optical fundamental is shown in Figures 5(a) and (b), respectively. The optical RMS increases monotonically with both i and Φ . The X-ray RMS drops to zero at inclinations between 45° and 65° , depending on Φ , where the light curve shows a double bump structure (thus, the harmonic here is non-zero). At higher inclinations RMS increases again. At high inclinations and large Φ in the shaded region, self-eclipses of the disk become possible, causing dramatic increase of RMS. The dot-dashed black line separates the regions, where the phase difference between the optical/X-ray fundamental QPOs shifts from 0 to π . Also the amplitude of the X-ray fundamental turns zero along this line.

Figures 5(c) and (d) present the contour plot of the harmonic RMS for X-rays and optical, respectively. Here the RMS is monotonically growing with both i and Φ up to rather large $i \gtrsim 70^\circ$ (i.e. $\sim 90^\circ - 2\beta$). At large inclinations eclipses become possible (see right panels of Figure 4). In that case, both RMS show very erratic behavior and depend strongly on i , first rapidly rising and then dropping to nearly zero (at somewhat different places of the plane shown by black dashed lines), but here the higher harmonics are strong. This is easily seen in Figures 5(e)–(g) which show the RMS behavior as a function of i for fixed Φ .

We see that, for the chosen parameters, the optical fundamental is stronger than the X-ray fundamental for all observer azimuths whereas the X-ray harmonic is nearly always stronger than the optical harmonic. Without eclipses, the optical harmonic is typically ten times

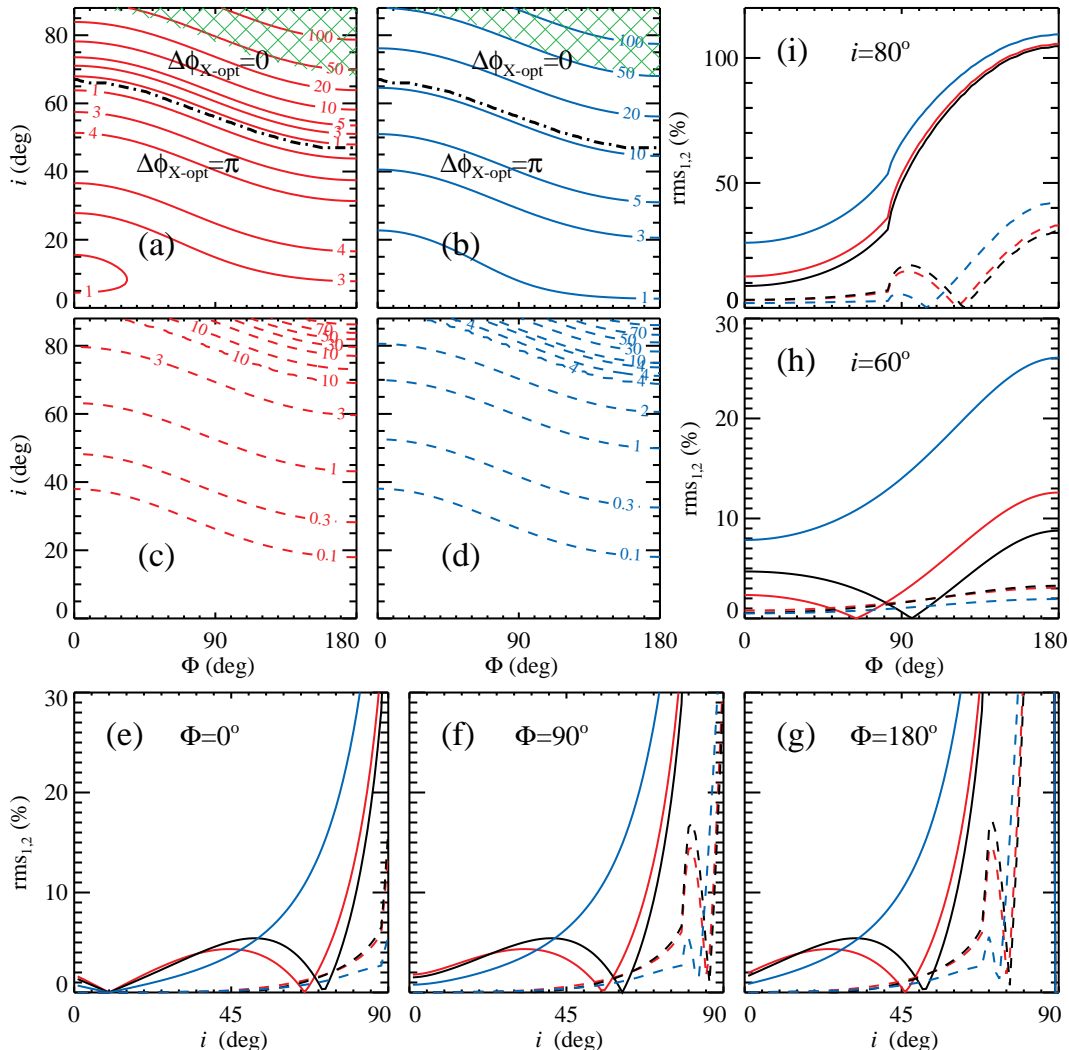


Figure 5. Fractional RMS amplitudes (in percent) as functions of i and Φ . The left-upper four panels present the contour plots for X-ray (a,c) and optical (b,d) fractional RMS amplitudes on the plane i - Φ . The upper panels (a and b) are for the fundamental, while the two lower panels (c and d) show the harmonic. Eclipses are possible in the shaded regions marked on the top panels. The dot-dashed black line separates the regions, where the phase difference between the optical/X-ray fundamental QPOs shifts from 0 to π . The amplitude of the X-ray fundamental turns zero along this line. Three bottom panels present the cross-section of these plots at the azimuthal angles $\Phi = 0^\circ$ (panel e), 90° (panel f), and 180° (panel g). The panels on the right show the cross-section at two inclinations $i = 60^\circ$ (panel h) and 80° (panel i). The X-rays (red curves) are assumed to originate from a hot disk extending from 3 to $30R_S$ emitting according to the standard emissivity profile given by equation (1), while the optical (blue curves) corresponds to a narrow ring at $R = 30R_S$. The solid curves present the RMS for the fundamental and the dashed curves give the harmonic. The RMS for the X-rays from a narrow ring at $R = 5R_S$ are shown in the panels (e-i) by black curves, which show similar behavior to the full hot flow case.

weaker than the fundamental, while the X-ray harmonic can be even stronger than the corresponding fundamental. For better visualization we also plot a cross-section of these contour plots in Figures 5(h) and (i) for two representative inclinations $i = 60^\circ$ and 80° , respectively. The first is the mean possible inclination of an arbitrary observer, while the second is chosen to show the role of eclipses. Here we additionally show the case of the X-rays from a narrow ring at $5R_S$ by black lines. In panel (h), we clearly see a drop of the fundamental X-ray RMS at $\Phi = 50$ – 100° and in panel (i) a rapid growth of RMS when eclipses become possible at $\Phi \sim 80^\circ$.

3. DISCUSSION

3.1. Comparison with observations

Our results show that the X-ray light-curves have strong harmonics, while optical harmonics are weaker for most of sets (i, Φ) . Indeed, harmonics are often found in the X-ray PSDs (e.g. Rodriguez et al. 2004), but no optical harmonics have been reported so far. This can also be seen in the (quasi-) simultaneous data of Motch et al. (1983, fig. 2), where both optical and X-ray PSDs show a QPO at ~ 0.05 Hz, two harmonics ~ 0.1 Hz and ~ 0.15 Hz are seen in the X-ray, but not in the optical PSD. Our simulations suggest that the RMS amplitudes of the fundamental harmonic in the optical are expected to be larger. Unfortunately, the data with both X-ray and optical QPOs detected are not strictly simultaneous, thus the PSDs are plotted in arbitrary units (Motch et al. 1983; Hynes et al. 2003). In the available simultaneous data of Swift J1753.5–0127, the optical

QPO is present with RMS=4–11%, while the upper limit on the X-ray QPO RMS at the same frequency is 3% (Durant et al. 2009). In GX 339–4 situation is similar, the optical QPO is present at RMS=3%, while the upper limit on the X-ray QPO RMS at the same frequency is 7.5% (Gandhi et al. 2010). This is consistent with our model which predicts that the X-ray QPO is there, just at a low RMS. On the other hand, we, of course, cannot rule out there being no QPO at all. In order to check the presence of the X-ray QPO in the data (which is related to the optical QPO), one may search for modulations at the corresponding frequency in the cross-correlation function. These oscillations are indeed present in the 2007 data on Swift J1753.5–0127 (see Durant et al. 2008, Veledina et al. in prep.) and hints of them can also be seen in the GX 339–4 data (Gandhi et al. 2010, fig. 21).

In Figure 1 we reproduced the range of possible QPO frequencies (the same for optical and X-rays) as a function of the hot flow outer radius. Since the dependence on parameters is not too strong, it is feasible to determine R_{out} for a given ν_{QPO} . In realistic situation, R_{out} fluctuates together with the mass accretion rate, leading to a change of the QPO frequency and broadening of the QPO features in the PSD. We note that the given frequencies were computed under the assumption of the rotation of the hot flow as a solid body, which breaks down for a large hot flow, limiting the outer radii, where the QPOs can be observed.

The lowest QPO frequencies ~ 0.05 Hz (optical) and ~ 0.03 Hz (X-rays) were observed in the hard state. According to Figure 1, we find the hot flow outer radius can be $\sim 100 R_S$, and even larger for $H/R > 0.4$ or spin $a > 0.5$. In this case, the optical and IR wavelengths are dominated by the radiation of the translucent parts of the hot flow (see e.g., Veledina et al. 2013, fig. 3: optical wavelengths are dominated by the radiation coming from $\sim 30 R_S$).

During the state transition, with the rise of the mass accretion rate, the outer shells of the hot flow are gradually replaced by the cold accretion disk (Esin et al. 1997, 1998; Poutanen et al. 1997). As the outer radius of the hot flow decreases, an increase of the QPO frequency occurs. This is seen in the data as correlated changes in the spectral slope and QPO frequency (see e.g. Gilfanov 2010), and expected in the precession model of Fragile et al. (2007) and Ingram et al. (2009). Simultaneously, a sharp drop of the IR radiation is expected, with fluxes at longer wavelengths dropping just before those at shorter wavelengths. While the cold accretion disk is sufficiently far away, the X-ray spectrum does not change significantly, as the amount of cold disk photons are not enough to make it softer. The noticeable X-ray spectral transition starts when the cold disk is rather close to the BH, at radii about $10 R_S$ (fig. 5 of Veledina et al. 2013). For such a small hot flow, IR wavelengths belong to the optically thick (self-absorbed) part of the spectrum, which is very hard, with spectral index up to $\alpha = 5/2$ ($F_\nu \propto \nu^\alpha$). Thus, in the hard-intermediate state we expect to see the QPO feature with frequencies $\gtrsim 1$ Hz in the near-IR, but not in the mid-IR or longer wavelengths, which would likely be very faint, probably, too faint to be detectable. The optical/X-ray phase lags in both translucent and opaque cases are expected to be the same (see below), either 0 or π depending on

the observer azimuthal angle and inclination. Maximum optical/near-IR QPO frequency in our model is the same as in the X-rays ~ 10 Hz (for a $10 M_\odot$ BH).

We discussed in detail the OIR QPOs produced only by the hot accretion flow, however these presumably may originate from other components, such as reprocessed X-ray radiation (for low QPO frequencies) and the jet (if it is entirely driven by the accretion flow). It is likely that the component giving major contribution to the observed flux also produces the QPOs, because of their rather large RMS. Simultaneous data of SWIFT J1753.5–0127 at late stages of the outburst (Durant et al. 2009, fig. 6, see also Chiang et al. 2010, fig. 5) suggest that the optical lies on the continuation of the X-ray power-law, as expected in the hot flow scenario (Veledina et al. 2013). Some irradiation may also play a role (as supported by the cross-correlation studies of Hynes et al. 2009 during the outburst peak), but the jet is very faint in this object. Thus the optical QPOs are likely produced by the hot flow. It is therefore suggestive that the hot flow scenario also works in other objects displaying QPOs, such as XTE J1118+480 and GX 339–4.

3.2. Unaccounted effects

Because we aimed to have as few parameters as possible, the model we consider is rather simplified. In a more realistic problem, a number of additional effects could also be accounted for, namely: the wavelength dependence of the optical profiles, occultations of the hot flow by the cold accretion disk, effects of the hot flow geometry, e.g. its finite and radius-dependent thickness, presence of the large-scale magnetic field, presence of other spectral components in the optical, such as the reprocessed emission and the jet. Let us now consider possible consequences of these effects.

1. The optical QPO profiles were calculated assuming these wavelengths belong to the partially self-absorbed regime. However, if the flow is small (e.g., $R \lesssim 10 R_S$), the optical (and even more certainly the IR) is likely to be in the self-absorbed part of the spectrum ($\tau_{\text{SA}} \gg 1$). In this case, the intensity of escaping radiation is isotropic and the flux depends only on the surface area of the flow projected to the line of sight modified by relativistic effects. The QPO waveforms in this case are not much different from the previously considered case of emission at the self-absorption frequency, but the RMS of the fundamental is somewhat larger and the harmonic is weaker.
2. For calculations of the X-ray QPO profiles, we adopted a simple prescription for the angular dependence of the specific intensity from the hot flow given by equation (8). Obviously, it is only an approximation to the real angular dependence that should be computed using the full Compton scattering kernel (see e.g. Poutanen & Svensson 1996). The intensity $I(\zeta')$ in reality should depend on the photon energy as well as on τ and temperature, with both being functions of the accretion rate and the distance from the BH. We do not expect that the general topology of the solution will change, but the details (e.g. the position of the line sep-

arating the phase lag $\Delta\phi_{X-opt} = 0$ and π in Figure 5) might differ. The result will also depend on the X-ray energy band.

3. Hard state BHBs are known to have radio jets (Fender 2006). Theoretical models for the jet launching require the presence of the large scale magnetic field. In that case, the synchrotron emissivity within the hot flow is no longer isotropic, but depends on the pitch angle α to the magnetic field as $\sin^2 \alpha$. This would lead to a different angular dependence of the escaping intensity. For a poloidal field, radiation would be more beamed along the hot flow surface leading to a luminosity angular dependence similar to that in the X-rays. In this case, the optical waveforms are expected to have more harmonic content.
4. Possible occultations of the hot flow by coverage of the inner parts of the cold accretion disk or by its flared outer parts may occur. These would lead to the asymmetry of the optical (and X-ray) QPO profiles and absence of the secondary peak in the X-ray profiles. Similarly to the considered occultations at high inclinations, this would lead to an increase of the fundamental RMS and harmonic content. Additionally, the optical and X-ray profiles will not be anymore in phase (or in anti phase).
5. We considered a simple case with a flat precessing disk, but in reality, the hot flow has finite thickness. This does not have much effect on the profiles for low inclinations. Self-eclipses of the hot flow will appear at somewhat lower inclinations, but, on the other hand, emission from the outer side of the hot flow will be visible and the eclipses will not be so deep. Thus, the increase in RMS will not be so significant and the harmonic content will be somewhat lower.
6. When estimating the RMS we assumed that the optical emission is produced entirely by the hot flow. In reality, additionally there is reprocessed emission from the outer disk that might be dominant at longer wavelengths as well as possibly optically thin, soft emission from the radio jet that might contribute to the emission at shorter wavelengths. These components not only contribute to the flux diluting the RMS from the hot flow, but also in principle can be variable at the QPO frequency. As reprocessing occurs in the outer part of the accretion disk, it acts as a low-pass filter (e.g. Veledina et al. 2011), reducing signal at high frequencies. Thus the reprocessing is not expected to vary at relatively high QPO frequencies. Whether the jet can produce QPOs at the same frequency as the inner hot flow precesses is not clear. The Lense-Thirring effect generally cannot cause the jet precession unless the jet is driven entirely by the accretion flow (Nixon & King 2013). Hence, the presence of several components in the spectrum typically will reduce the RMS amplitude of the optical QPO by a factor $1 + r$, where $r = (F_{E,jet} + F_{E,repr})/F_{E,hf}$ is the ratio of the ob-

served fluxes at a given energy produced by the jet and reprocessing to that of the hot flow.

4. SUMMARY

A number of BH binaries have recently been found to show QPO features in their optical PSDs. Recently, it has been shown that similar QPOs in the X-rays are well explained by Lense-Thirring precession of the hot accretion flow. Here we propose that OIR QPOs originate from the same process, namely that the outer parts of the precessing hot flow are radiating in the optical (by non-thermal synchrotron), producing QPOs at frequencies matching those in the X-rays.

We calculate the possible OIR profiles and make predictions for the phase difference with the X-rays. The phase shift can be either 0 (at high inclinations) or π (at low inclinations), with the boundary between these cases depending on the azimuthal angle of the observer. We also investigate the harmonic content and show dependence of the RMS on parameters for two first harmonics. Here we show that the X-ray QPOs should have smaller RMS at the fundamental frequency than the OIR QPOs. On the other hand, the X-ray QPOs should have much stronger harmonic.

We discuss possible QPO frequencies and their connection to the broadband spectral properties. At the hard-to-soft state transition we expect the OIR QPO frequency to increase, always being the same as in the X-rays, up to ~ 10 Hz in the hard-intermediate state. The broadband spectrum is expected to change in such a way that the emission at longer wavelengths drops before the subsequent drop at shorter wavelengths (infrared, optical). After that the X-ray transition occurs. In the hard state, the QPO feature is sometimes absent (not significant) in the X-ray PSD, but detected in the optical. Their common origin can be established through the cross-correlation analysis, where the oscillations at corresponding frequency can be present. Using future X-ray missions with high time-resolution capability, such as *LOFT*, together with the corresponding high time-resolution instruments in the optical, we will be able to confirm or discard this.

This work was supported by the Finnish Graduate School in Astronomy and Space Physics (AV).

REFERENCES

- Bardeen, J. M. & Petterson, J. A. 1975, *ApJ*, 195, L65
 Belloni, T., Psaltis, D., & van der Klis, M. 2002, *ApJ*, 572, 392
 Casella, P., Maccarone, T. J., O'Brien, K., et al. 2010, *MNRAS*, 404, L21
 Chiang, C. Y., Done, C., Still, M., & Godet, O. 2010, *MNRAS*, 403, 1102
 Dexter, J. & Agol, E. 2009, *ApJ*, 696, 1616
 Done, C., Gierliński, M., & Kubota, A. 2007, *A&A Rev.*, 15, 1
 Durant, M., Gandhi, P., Shahbaz, T., et al. 2008, *ApJ*, 682, L45
 Durant, M., Gandhi, P., Shahbaz, T., Peralta, H. H., & Dhillion, V. S. 2009, *MNRAS*, 392, 309
 Esin, A. A., McClintock, J. E., & Narayan, R. 1997, *ApJ*, 489, 865
 Esin, A. A., Narayan, R., Cui, W., Grove, J. E., & Zhang, S.-N. 1998, *ApJ*, 505, 854
 Fender, R. 2006, in *Compact stellar X-ray sources*, Cambridge Astrophysics Series, No. 39, ed. W. H. G. Lewin & M. van der Klis (Cambridge: Cambridge University Press), 381
 Fragile, P. C. 2009, *ApJ*, 706, L246
 Fragile, P. C., Blaes, O. M., Anninos, P., & Salmonson, J. D. 2007, *ApJ*, 668, 417

- Gandhi, P., Dhillon, V. S., Durant, M., et al. 2010, *MNRAS*, 407, 2166
- Gilfanov, M. 2010, in *Lecture Notes in Physics*, Vol. 794, *The Jet Paradigm*, ed. T. Belloni, Berlin, 17
- Hynes, R. I., Haswell, C. A., Cui, W., et al. 2003, *MNRAS*, 345, 292
- Hynes, R. I., O'Brien, K., Mullally, F., & Ashcraft, T. 2009, *MNRAS*, 399, 281
- Imamura, J. N., Kristian, J., Middleditch, J., & Steiman-Cameron, T. Y. 1990, *ApJ*, 365, 312
- Ingram, A. & Done, C. 2011, *MNRAS*, 415, 2323
- Ingram, A., Done, C., & Fragile, P. C. 2009, *MNRAS*, 397, L101
- Kanbach, G., Straubmeier, C., Spruit, H. C., & Belloni, T. 2001, *Nature*, 414, 180
- Kato, S., Fukue, J., & Mineshige, S. 2008, *Black-Hole Accretion Disks – Towards a New Paradigm* (Kyoto: Kyoto University Press)
- Kumar, S. & Pringle, J. E. 1985, *MNRAS*, 213, 435
- Lubow, S. H., Ogilvie, G. I., & Pringle, J. E. 2002, *MNRAS*, 337, 706
- Malzac, J. & Belmont, R. 2009, *MNRAS*, 392, 570
- Motch, C., Ilovaisky, S. A., Chevalier, C., & Angebault, P. 1985, *Space Sci. Rev.*, 40, 219
- Motch, C., Ricketts, M. J., Page, C. G., Ilovaisky, S. A., & Chevalier, C. 1983, *A&A*, 119, 171
- Nixon, C. & King, A. 2013, *ApJ*, 765, L7
- Novikov, D. I. & Thorne, K. S. 1973, in *Black Holes (Les Astres Occlus)*, ed. C. Dewitt & B. S. Dewitt (New York: Gordon & Breach), 343
- Papaloizou, J. C. B. & Pringle, J. E. 1983, *MNRAS*, 202, 1181
- Poutanen, J. & Beloborodov, A. M. 2006, *MNRAS*, 373, 836
- Poutanen, J. & Gierliński, M. 2003, *MNRAS*, 343, 1301
- Poutanen, J., Krolik, J. H., & Ryde, F. 1997, *MNRAS*, 292, L21
- Poutanen, J. & Svensson, R. 1996, *ApJ*, 470, 249
- Poutanen, J. & Vurm, I. 2009, *ApJ*, 690, L97
- Remillard, R. A. & McClintock, J. E. 2006, *ARA&A*, 44, 49
- Remillard, R. A., McClintock, J. E., Sobczak, G. J., Bailyn, C. D., Orosz, J. A., Morgan, E. H., & Levine, A. M. 1999, *ApJ*, 517, L127
- Rodriguez, J., Corbel, S., Kalemci, E., Tomsick, J. A., & Tagger, M. 2004, *ApJ*, 612, 1018
- Schnittman, J. D., Homan, J., & Miller, J. M. 2006, *ApJ*, 642, 420
- Shakura, N. I. & Sunyaev, R. A. 1973, *A&A*, 24, 337
- Steiman-Cameron, T. Y., Scargle, J. D., Imamura, J. N., & Middleditch, J. 1997, *ApJ*, 487, 396
- Stella, L. & Vietri, M. 1998, *ApJ*, 492, L59
- Sunyaev, R. A. & Titarchuk, L. G. 1985, *A&A*, 143, 374
- Veledina, A., Poutanen, J., & Vurm, I. 2011, *ApJ*, 737, L17
- . 2013, *MNRAS*, 430, 3196
- Viironen, K. & Poutanen, J. 2004, *A&A*, 426, 985
- Vikhlinin, A., Churazov, E., Gilfanov, M., et al. 1994, *ApJ*, 424, 395
- Wagoner, R. V., Silbergleit, A. S., & Ortega-Rodríguez, M. 2001, *ApJ*, 559, L25
- Wijnands, R. & van der Klis, M. 1999, *ApJ*, 514, 939
- Zdziarski, A. A. & Gierliński, M. 2004, *Prog. Theor. Phys. Suppl.*, 155, 99